Preparation of solid solution and layered IrO_x-$Ni(OH)_2$ oxygen evolution catalysts: Towards optimising iridium efficiency for OER.

Jonathan Ruiz Esquius[a], Gerardo Algara-Siller[b], Ioannis Spanos[c], Simon J. Freakley[a,d], Robert Schlögl[b,c] and Graham J. Hutchings[*a]

[a] School of Chemistry, Cardiff Catalysis Institute, Cardiff University, Main Building, Park Place, Cardiff CF10 3AT, UK.

[b] Department of Inorganic Chemistry, Fritz-Haber-Institut der Max-Planck-Gesellschaft, Faradayweg 4-6, 14195, Berlin, Germany.

[c] Department of Heterogeneous Reactions, Max Planck Institute for Chemical Energy Conversion, Stiftstrasse 34-36, Mulheim an der Ruhr, 45470, Germany.

[d] Department of Chemistry, University of Bath, Claverton Down, Bath, BA2 2AY, UK.

* Hutch@cardiff.ac.uk

Abstract

Minimising iridium loading in oxygen evolution reaction (OER) catalysts, without impairing electrocatalytic activity and stability is crucial to reduce the cost of water electrolysis. In this work, two $Ir_{0.5}Ni_{0.5}O_x$ mixed oxide catalysts with layered and solid solution morphologies were prepared by modifying a facile hydrothermal methodology. The catalytic OER activity and stability for the Ir-Ni catalyst with a homogeneous distribution (IrNi-HD) was seriously compromised compared to pure IrO_x due to the high concentration of surface nickel prone to corrosion under reaction conditions. Whilst, the design of layered IrO_x-$Ni(OH)_x$ (IrNi-LY), with Ir at the exposed surface, allowed a 50 % molar reduction in the concentration of precious metal on the electrode compared to IrO_x without impairing the catalytic activity or stability. As a result, IrNi-LY outperformed IrO_x in activity when normalised to the Ir mass.

Keywords: electrocatalysis, oxygen evolution reaction, iridium oxide, amorphous iridium oxo-hydroxide, hydrothermal synthesis, iridium nickel mixed oxide.

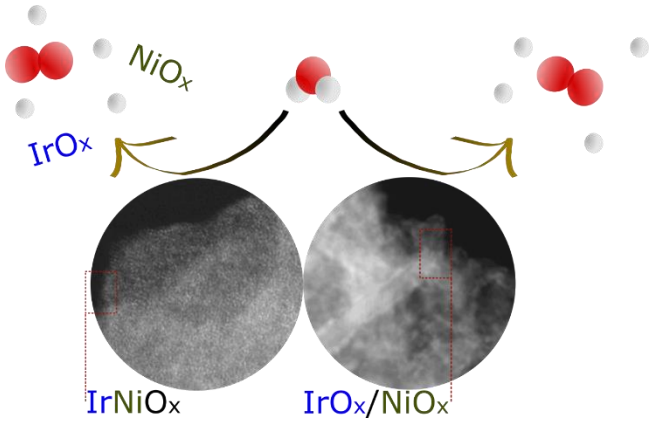

Introduction

At present 17 TW of energy is consumed annually worldwide, of which approximately 90 % is produced from finite fossil resources.[1,2] Considering the annual population growth (2-3%) and the projected annual economic growth (2-5%), global energy consumption is expected to increase between 4-8% per year, and thus it is foreseen that global energy consumption will reach 30 TW by 2050.[1,2] Fossil fuel derived CO_2 is harmful to the climate,[3] and hence, to meet the future energy demand and minimise adverse climate change, energy production needs to approach being CO_2 neutral. Hydrogen derived from water electrolysis is a possible green energy vector and an alternative to carbon-based fuels (natural gas, coal or oil).

Polymer electrolyte membrane (PEM) technology allows storage of surplus energy produced from renewables in the form of hydrogen *via* water splitting. The bottleneck of PEM technology is that IrO_2-based catalysts are virtually the only feasible anode materials for the oxygen evolution reaction (OER), half of the water electrolysis process. Iridium is among the scarcest elements on Earth, obtained as a by-product in the mining of other precious metals.[2] Therefore, for PEM technology to succeed and fulfil the hydrogen production demand, iridium needs to be used efficiently.

The addition of nickel and other base metals into the IrO_2 lattice, to form a mixed oxide catalyst, has been used to improve iridium dispersion and activity for the OER. Reier *et al*.[4] prepared $Ir_xNi_{1-x}O_2$ mixed oxide films with a homogenous metal distribution *via* thermal decomposition of metal acetates at 450 °C. At 1.53 V_{RHE} the current density of 1 $mA \cdot cm^{-2}$ for IrO_2 progressively increased to 7 $mA \cdot cm^{-2}$ with increasing nickel content to $Ir_{0.33}Ni_{0.67}O_2$. However, the dissolution of iridium increased dramatically with increasing nickel content, and thus, the observed gain in activity was at the expenses of the catalyst stability.[4] Moghaddam *et al*.[5] prepared $IrNi_xO_y$ mixed oxide catalyst via a hydrothermal synthesis. On addition of nickel, the initial current density of 85 $A \cdot g_{Ir}^{-1}$ for pure IrO_x, increased linearly to 142 $A \cdot g_{Ir}^{-1}$ for $IrNi_{0.125}O_y$, without impairing the catalyst stability (1 $mA \cdot cm^{-2}$, 3 h), nevertheless, further increasing the nickel loading led to progressive deactivation. These results suggest that a homogeneous metal distribution with the addition of high concentrations of Ni compromises catalyst stability. This was attributed to the dissolution of surface nickel leading to the formation of highly exposed and undercoordinated iridium centres which initially provide more active species but are prone to corrosion.[4] Therefore, the formation of heterogeneous structures, e.g. core-shell or sandwich-like structures, with iridium at the outer surface is preferred to a homogeneous metal distribution in order to reduce the overall amount of iridium in these

materials. Nong *et al*.[6,7] prepared IrNi mixed oxide catalysts *via* a polyol method with a homogeneous Ir-Ni distribution, nickel was subsequently dealloyed from the surface to form the IrO_x shell and an IrNi-core. Following this approach, a catalyst with 3.3 moles of nickel per mole of iridium was developed with higher activity than pure IrO_2 (37 $A \cdot g_{Ir}^{-1}$ and 12 $A \cdot g_{Ir}^{-1}$ at 1.48 V_{RHE} respectively) and comparable stability (1 $mA \cdot cm^{-2}$, 3 h).[6] Similar results were obtained by Papaderakis *et al*.[8] on Ir-shell IrNi-core catalysts prepared by galvanic replacement, where the current density increased from 7 $mA \cdot cm^{-2}$ to 20 $mA \cdot cm^{-2}$ after the incorporation of 17-22 at. % nickel.

Amorphous iridium oxo-hydroxides (IrO_x) have improved activity towards OER compared to crystalline rutile IrO_2,[9,10] this is suggested to be because of the presence of Ir(III)/Ir(IV) and electrophilic O^- sites (electron holes in the O(2p) orbital),[11] induced by Ir(IV) vacancies in the lattice.[12] Operando X-ray absorption spectroscopy (XAS) confirmed the presence of electrophilic oxygen sites, produced as a result of iridium vacancies in Ir@$IrNiO_x$ catalyst formed after Ni-dealloying.[13]

As previously reported,[6–8,14] Ir@IrNi core-shell catalysts allow the reduction of iridium on the electrode whilst increasing IrO_2 efficiency towards OER. However, through the formation of an IrNi core and an outer Ir-shell utilisation of Ir is not fully optimised. In this communication, amorphous $Ir_{0.5}Ni_{0.5}O_x$ catalysts with a homogenous metal distribution (IrNi-HD) or with a sandwich-like structure formed by $NiO_x/Ni(OH)_x$ nanosheets encapsulated with an IrO_x layer (IrNi-LY) were synthesised following a modification of a facile hydrothermal synthesis previously described for IrO_x.[5,15] The aim of this work is to highlight the benefits of a layered structure with surface IrO_x, compared to a homogenous metal distribution, in significantly lowering the required iridium loading on the electrode to achieve similar activity and selectivity towards OER. Moreover, the flexibility of this preparation of a $NiO_x/Ni(OH)_x$-inner nanomaterial rather than a IrNi-containing core,[6–8,13,14] allows for further optimisation of Ir usage in OER electrodes.

Methods

Materials

All chemicals were purchased from commercial suppliers and used as received. Iridium chloride hydrate ($IrCl_3 \cdot 3H_2O$ 99 %, Sigma Aldrich), nickel chloride hexahydrate ($NiCl_2 \cdot 6H_2O$ 99.9 %, Sigma Aldrich), lithium carbonate (Li_2CO_3 99 %, Fisher Chemicals), perchloric acid ($HClO_4$ 70 % in water, Honeywell Fluka), 5% perfluorinated resin solution (Nafion® solution, Sigma Aldrich), Ethanol (100 %, VWR Chemicals).

IrO_x synthesis

The preparation of IrO_x was described previously in literature[15] and is as follows: 1 mmol of $IrCl_3$ hydrate (299 mg) and 8 mmol of base (591 mg of Li_2CO_3) were dissolved in a 50 ml round bottom flask with 10 ml of deionised water and stirred for 16 h at room temperature. A further 10 ml of deionised water was then added to the solution after this initial period followed by heating to reflux for 3 hours. A blue precipitate was observed, which was recovered by filtration and washed with 1 L of cold deionised water and 1 L of hot deionised water. Finally, the material was dried at room temperature for 16 h.

$Ir_{0.5}Ni_{0.5}O_x$ with a solid solution distribution synthesis (IrNi-HD)

0.5 mmol of $IrCl_3$ hydrate (149 mg), 0.5 mmol of $NiCl_2$ hexahydrate (119 mg) and 8 mmol of Li_2CO_3 (591 mg) were dissolved in 10 ml of deionised water and stirred for 16 h at room temperature in a 50 ml round bottom flask. A further 10 ml of deionised water was then added to the solution followed by heating to reflux for 3 hours. A blue precipitate was observed which was recovered by filtration and washed with 1 L of cold deionised water and 1 L of hot deionised water. The material was dried at room temperature for 16 h.

$Ir_{0.5}Ni_{0.5}O_x$ with layered structure (IrNi-LY)

For the preparation of $Ir_{0.5}Ni_{0.5}O_x$ with NiO_x nanosheets covered with a layer of IrO_x two precursors solutions were prepared separately before mixing. 0.5 mmol of $IrCl_3$ hydrate (149 mg) and 4 mmol of Li_2CO_3 (295 mg) were dissolved in 10 ml of deionised water and stirred at room temperature for 16 hours. 0.5 mmol of $NiCl_2$ hydrate (119 mg) and 4 mmol of LiOH (96 mg) was dissolved in 10 ml of deionised water and stirred overnight at room temperature for 16 h in a second flask. The latter solution was heated to 95 °C for 30 min, then the $IrCl_3$ solution was added drop-wise to the $NiCl_2$ solution. After the addition, the mixture was heated to reflux for 1.5 h. A precipitate formed which was recovered by filtration and washed with 1 L of cold water and 1 L of hot water. Finally, the catalyst was dried at room temperature for 16 h.

Catalyst characterisation

Powder X-ray diffraction (XRD) were performed on a (θ-θ) X'PertPro Panalytical instrument fitted with a hemispherical analyser using a Cu Kα radiation (1.5406 Å) source (40 keV, 40 mA). X-ray photoelectron spectroscopy (XPS) were recorded on a Kratos Axis Ultra DLD XPS spectrometer equipped with an Al Kα X-ray source (140 W, 1486.6 eV), data was analysed using Casa XPS software. Microwave plasma atomic emission

spectroscopy (MP-AES) were recorded on an Agilent Technologies 4100. The X-ray absorption fine structure (XAFS) for catalyst loaded on carbon cloth (Sigracet 39 AA) were recorded in fluorescence mode at Ir L_3 edge, at B18 beamline of the Diamond Light Source, at Harwell, UK. *In situ* measurements were acquired using a closed cell described previously in literature[16] in fluorescence mode, filled with $HClO_4$ (0.1 M), a Pt wire and a Ag/AgCl electrode was used as the counter and reference electrode respectively. 5 scans were recorded at each potential, the average signal was used for data analysis. X-ray absorption near-edge structure (XANES) and X-ray absorption fine structure (EXAFS) data analysis was performed using IFEFFIT with Demeter software package (Athena and Artemis).[17] Electron microscopy characterisation and energy dispersive X-ray spectroscopy were performed in a JEOL JEM-ARM200F and a FEI Talos F200X transmission electron microscopy (TEM), both microscopes operated at 200 kV.

Catalyst testing

The preparation of the catalyst ink is as follows: 5 mg of grinded catalyst were re-dispersed in 1.23 mL of water, 1.23 mL of ethanol and 40 µl of nafion solution. The mixture was sonicated for 30 min in order to ensure the complete re-dispersion of the material. To obtain a catalyst loading of 100 $\mu g \cdot cm^{-2}$, 10 µl of the catalyst ink was drop-cast onto the working electrode and dried under a N_2 flow for 30 min.

Electrochemical measurements were recorded on a conventional 3-electrode cell in 0.1 M $HClO_4$ electrolyte. A coiled Pt wire (127 µm diameter, 99.99 %, Sigma Aldrich) was used as counter electrode, a glassy carbon tip of 0.196 cm^2 area was used as the working electrode and a calomel electrode ([Cl^-/Hg_2Cl_2/Hg/Pt], IJ Cambria Scientific Ltd, model CHI-150) as the reference. The intrinsic catalysts activity towards OER was measured by linear sweep voltammetry (LSV, 1.20 V_{RHE} to 1.65 V_{RHE} at 5 $mV \cdot s^{-1}$) and the catalysts stability was assessed by chronopotentiometry (CP, 2 h at 10 $mA \cdot cm^{-2}$). Iridium and nickel corrosion during CP were recorded on a 3-electrode flow cell reactor (1.2 $ml \cdot min^{-1}$, 0.1 M $HClO_4$) coupled with an ICP described previously in literature.[18] Reported results are expressed against the reversible hydrogen electrode (RHE).

Results and Discussion

Characterisation of $IrNiO_x$ materials

Two $Ir_{0.5}Ni_{0.5}O_x$ catalysts; homogeneously distributed (IrNi-HD) and layered (IrNi-LY), were prepared *via* hydrothermal synthesis. Under strong aqueous alkaline conditions the

metal chloride precursors, $IrCl_3 \cdot 3H_2O$ and $NiCl_2 \cdot 6H_2O$, are hydrolysed to $Ir(OH)_6^{3-}$ and $Ni(OH)_2$ (Eq. 1 and Eq. 4 respectively) and, upon heating condense to oxo-hydroxide oligomers (Eq. 2 and 5) which can precipitate or evolve to oxo-hydroxides (Eq. 3 and 6).[19–22]

$$Ir(H_2O)_3Cl_3 + 6\ OH^- \rightarrow [Ir(OH)_6]^{3-} + 3\ Cl^- + 3\ H_2O \quad \text{Eq. 1}$$

$$n\ [Ir(OH)_6]^{3-} \rightarrow Ir_nO_m + m\ H_2O + 6n\ OH^- \quad \text{Eq. 2}$$

$$Ir_nO_m + O_2 \rightarrow n\ IrO_x \quad \text{Eq. 3}$$

$$NiCl_2 + 2\ OH^- \rightarrow Ni(OH)_2 + 2\ Cl^- \quad \text{Eq. 4}$$

$$y\ Ni(OH)_2 \rightarrow Ni_yO_z + 2z\ H_2O \quad \text{Eq. 5}$$

$$Ni_yO_z + O_2 \rightarrow NiO_x \quad \text{Eq. 6}$$

Both precursors were added simultaneously to the same flask for the synthesis of IrNi-HD, whilst nickel oxo-hydroxide nanosheets were formed separately before the precipitation of a IrO_x layer in the presence of the NiO_x precipitate, to obtain the IrNi-LY catalyst. The theoretical Ir to Ni molar ratio of the materials with nominal composition $Ir_{0.5}Ni_{0.5}O_x$ was confirmed as $Ir_{0.51}Ni_{0.49}$ for both $Ir_{0.5}Ni_{0.5}$-LY and $Ir_{0.5}Ni_{0.5}$-HD catalysts by MP-AES.

Apart from synthesized IrNi-HD and IrNi-LY mixed oxide catalysts, an amorphous IrO_x catalyst was synthesised for comparison following the same methodology.[15] X-ray diffraction and transmission electron microscopy were used to characterise the synthesised samples. The general morphological description of the IrO_x and IrNi-HD samples is that they were amorphous (Figure S1a and S1b, respectively). However, adventitious contamination for IrNi-HD was observed in the form of small TiO_2 crystals found seldom in the sample (Figure S1c). The IrNi-LY is in turn a more ordered material as observed by the more defined signal and peak intensity in electron diffraction profile compared to IrO_x and IrNi-HD (Figure S2). The ordered phase was identified as layered $Ni(OH)_2$ (Figure 1a and 1b) with a probably interstratification of α/β-$Ni(OH)_2$[23] phases as suggested by the range of interlayer spacing lattice parameters. The layered $Ni(OH)_2$ is covered with an Ir-rich material, being this either amorphous agglomerations, clusters or semicrystalline nanoparticles (Figure 1c). The accurate elemental distribution of this iridium rich phase on the surface of IrNi-LY could not be resolved by energy dispersive X-ray spectroscopy due to radiation damage limitations and the complexity of the phase

itself. The XRD pattern recorded for IrO_x showed broad-low intensity reflections around 34° and 60° commonly reported for amorphous iridium oxo-hydroxides[19,24–28] in agreement with TEM characterisation. As expected from the precipitation step occurring in aqueous solution, and the lack of heat treatment in the drying process, no rutile IrO_2 (JCPDS-015-0876) or NiO (JCPDS 004-0835) were observed by XRD for synthesised catalysts (Figure S3).

Thorough characterisation of commercially available rutile IrO_2 and amorphous $IrO_2{\cdot}2H_2O$, from Sigma Aldrich and Alfa Aesar respectively, was described elsewhere.[9,12,15] Rutile IrO_2 was formed exclusively of Ir^{4+} and O^{2-} sites, whilst Ir^{3+}/Ir^{4+} sites were present in $IrO_2{\cdot}2H_2O$. In previous studies, we thoroughly characterised commercially sourced rutile IrO_2 and $IrO_2{\cdot}2H_2O$ by XPS,[29] the Ir($4f_{7/2}$) peak for rutile IrO_2 was centred at 61.9 eV with a characteristic FWHM of 0.70 eV.[29] Nevertheless, the presence of Ir^{3+} sites on amorphous iridium oxo-hydroxides caused the Ir(4f) peak to shift upwards in energy to 62.5 eV and to broaden (FWHM of 1.6 eV). Due to the Ir(4f) and O(1s) asymmetry,[30] overlapping of Ir(4f)/Ir(5p) orbitals and, electron correlation spin-orbit coupling[31,32] the Ir(4f) peak interpretation is complex. Additionally, for Ir-Ni mixed oxides overlap between Ir($4f_{7/2}$) and Ni(3p) must be taken into consideration.[33] To avoid misinterpretation, the Ir(4f) line for IrNi-HD and IrNi-LY was not fitted and discussion is based on the peak envelope curve.

The presence of surface carbon species, likely because of CO_3^{2-} decomposition from Li_2CO_3 used during the synthesis, was detected for all three catalysts. Hence other elements analysed by XPS were calibrated against the C(1s) at 284.8 eV. No chloride or lithium contamination was detected by XPS in the fresh samples. The Ir(4f) peak for IrO_x was centred at 62.2 eV (Figure 2a) with a FWHM value of 1.5 eV, consistent with previously reported amorphous materials[29] and supported by XRD and TEM. For IrNi-HD and IrNi-LY catalysts, overlap between Ir($4f_{7/2}$) and Ni(3p) at 61.9 eV and 67.3 eV[33] respectively adds to the complexity of Ir(4f) peak interpretation. For IrNi-HD, a distinct peak-shoulder corresponding to Ni(3p) was not observed on the Ir(4f) region, instead the presence of Ni was evidenced by a 0.6 eV shift towards higher binding energy compared to IrO_x and a slight peak broadening in the Ni(3p) region at 67.3 eV. Thus, the electronic structure of IrO_x was altered by the close proximity of Ni atoms, in agreement with the hypothesis that Ir and Ni oxo-hydroxide form a solid solution.[4] Nevertheless, for IrNi-LY the Ir(4f) peak position was unaltered compared to IrO_x, whilst nickel was observed as a distinct shoulder at 67.4 eV. This indicates that the electronic structure of iridium is not being altered by nickel, in accordance with a morphology where both metal oxides are separated. The difference in surface composition between $Ir_{0.5}Ni_{0.5}O_x$ catalysts with an

iridium and nickel homogeneous distribution or a layered structure was evidenced by XPS quantification. As shown in Table 1, composition for IrNi-HD approached the theoretical equimolar metal concentration, in good agreement with an iridium and nickel homogenous distribution throughout the material. Whereas iridium enrichment was observed for IrNi-LY, indicating a higher concentration of iridium at the surface compared to nickel, in good agreement with a layered distribution as observed by STEM.

Three oxygen species were detected on the O(1s) region of synthesised IrO_x (Figure 2b); oxide within the lattice at 530.2 eV, surface hydroxide groups at 531.1 eV and adsorbed water/carbonates from the base and the solvent at 532.4 eV.[29,34] Oxide, hydroxide and water/carbonates were also detected for the two synthesised IrNi mixed oxide catalysts (Figure 2b). As shown in Table 1, comparable oxygen speciation was observed for IrO_x and IrNi-LY catalysts, evidencing the similarity between both surfaces and further suggesting the formation of an IrO_x layer onto NiO_x nanosheets for IrNi-LY catalyst. Compared to IrO_x, a less oxidic surface was observed for IrNi-HD catalyst. This, in accordance with previous XPS characterisation performed by Reier *et al*.[4] on $Ir_xNi_{1-x}O_2$ films with a homogeneous metal distribution, where the addition of nickel within the IrO_2 lattice resulted in a shift in the oxygen speciation from oxide to hydroxide.

The interpretation of nickel by XPS is challenging due to its characteristic line shape, which cannot be defined by using a simple component in the fit.[35] Biesinger *et al*.[35] developed a multicomponent Ni(2p) peak fitting model for the quantification of Ni^0, $Ni(OH)_2$ and NiO, this method was used to identify the nickel speciation in synthesised $Ir_{0.5}Ni_{0.5}O_x$ catalysts. The analysis of the Ir(4f) spectra showed no electronic interaction between iridium and nickel on the catalyst with a layered distribution, therefore, no intermetallic interactions are expected on the Ni(2p) for IrNi-LY. As expected from the preparation procedure, the absence of a reducing agent resulted in no Ni metal. The $Ni(2p_{3/2})$ for IrNi-LY is centred at 855.5 eV suggesting that most of the nickel is present as $Ni(OH)_2$, applying the peak fitting reported previously in literature,[35] it was confirmed that NiO contributed approximately to only the 8 % of the Ni(2p) envelope whilst the remaining 92 % was attributed to $Ni(OH)_2$ (Figure 2c). For IrNi-HD, nickel modified the electronic structure of iridium oxide, as observed by the 0.6 eV shift towards higher binding energy on the Ir(4f) line. Congruently, the electronic structure of nickel is perturbed by the close proximity of iridium, as observed by the 0.7 eV shift towards higher binding energy of the Ni(2p) spectrum.[36] Peak components used in the fitting of IrNi-HD were shifted 0.7 eV towards higher binding energy compared to IrNi-LY, in accordance with the peak envelope shift. The peak associated to NiO increased its contribution to 33 % whilst the $Ni(OH)_2$ proportion decreased to 67 %.

To further explore electronic and structural changes in IrO_x induced by the incorporation of nickel, the iridium L_3 edge (2p to 5d electronic transition) was investigated by X-ray absorption spectroscopy (XAS). To compare the relative oxidation state between samples, the position, intensity and shape of the X-ray absorption near edge structure (XANES) was analysed. For more accurate comparison, commercial rutile IrO_2, from Sigma Aldrich, which has been thoroughly characterised in literature,[9,10] was employed as reference, since it was confirmed to be composed exclusively of Ir^{4+} sites.[11] Further characterisation for rutile IrO_2 by XRD, XPS and electrochemical methods can be obtained in the supplementary information (Figure S4 and Figure S5). Normalised XANES spectra at Ir L_3 edge for rutile IrO_2 and synthesised samples are shown in Figure 3. The white line position for IrO_x, IrNi-HD and IrNi-LY was shifted towards lower energy compared to rutile IrO_2, indicating an average oxidation state lower than Ir^{4+}, in agreement with the coexistence of Ir^{3+} and Ir^{4+} sites observed by XPS and, as commonly reported on amorphous IrO_x[34,37] and IrNi mixed oxide[38,39] catalysts. IrO_x and IrNi-LY show similar XANES spectras, indicating that the electronic structure of IrO_x was not significantly altered by the presence of nickel and, that iridium in IrNi-LY is similar to highly active oxo-hydroxide materials.

The first coordination shell of the extended X-ray absorption fine structure (EXAFS) was fitted using four equatorial Ir-O bonds and two axial Ir-O bonds (Table S1), fitted Ir-O bond distances are shown in Table 2. The average Ir-O bond distance for commercial rutile IrO_2 was 1.98 Å, in good agreement with previous XAS analysis.[34,40] A distortion of the rutile IrO_6 octahedra, with longer Ir-O and shorter Ir-Ir bond distances, was reported for amorphous iridium oxo-hydroxides,[26,34,37] which was attributed to the presence of Ir^{3+} and Ir^{4+} sites in the lattice. Longer Ir-O bond distances for IrO_x, IrNi-HD and IrNi-LY compared to rutile IrO_2, further agrees with the coexistence of Ir^{3+}/Ir^{4+} sites, as previously indicated by XPS and XANES characterisation. In addition to the slightly longer Ir-O bond distances observed for synthesised samples compared to rutile IrO_2 (Table 2), dampened signal above the first coordination shell suggests a more disordered structure than rutile IrO_2 (Figure 4), as evidenced by TEM and XRD.

Catalytic activity towards OER

The intrinsic catalytic activity and stability of synthesised catalysts towards OER was determined by LSV (1.20 to 1.65 V_{RHE} at 5 $mV \cdot s^{-1}$) and CP (10 $mA \cdot cm^{-2}$, 2 h) (Table 3). Synthesised IrO_x showed high intrinsic activity by LSV (51.5 $mA \cdot cm^{-2}$ at 1.58 V_{RHE}), and stability by CP (11 $mV \cdot h^{-1}$ degradation rate), comparable to results reported previously in literature.[41,42] Nickel oxide on its own is less active towards OER than iridium and not

stable against corrosion in acid media.[43] Hence it is expected that a high concentration of nickel at the surface would have a detrimental effect on the catalytic performance, as observed for IrNi-HD catalyst (Figure 5a), where an equimolar amount of Ni and Ir at the surface resulted in a current density 35 $mA \cdot cm^{-2}$ lower than IrO_x at the same potential (1.58 V_{RHE}). Moreover, surface nickel dissolution during OER may compromise the overall catalyst stability, likely due to catalyst delamination from the electrode,[44] as observed by the high degradation rate of 160 $mV \cdot h^{-1}$ observed by CP (Figure 5b). Due to the high concentration of surface Ni, adventitious TiO_2 contamination detected by TEM is not expected to play a crucial role in IrNi-HD activity or stability.

OER occurs at the surface of the catalyst meaning that iridium utilisation can be optimised by minimising the amount of iridium that is inaccessible in the bulk of the material. This can be achieved through catalyst design, concentrating IrO_x at the surface. XPS and TEM characterisation indicated that the surface of IrNi-LY is predominantly an IrO_x-rich phase, further supported by the similarity in performance of IrNi-LY and IrO_x by LSV (Figure 5a). Cyclic voltammetry (0.3 - 1.4 V_{RHE}, 50 $mV \cdot s^{-1}$) was employed to obtain information about catalytically active species present at the surface of the catalyst. The Ir^{3+}/Ir^{4+} and Ir^{4+}/Ir^{5+} redox events were observed at 0.90 V_{RHE} and 1.25 V_{RHE} for IrO_x and IrNi-LY catalysts,[45,46] whilst no redox processes were observed for IrNi-HD (Figure S6), which can be associated with the high concentration of nickel at the surface of the catalyst. CV curves suggest that the concentration of surface Ir^{3+} sites on IrNi-LY is comparable to IrO_x.[45] Tafel slopes for IrO_x (41 $mV \cdot dec^{-1}$), IrNi-LY (37 $mV \cdot dec^{-1}$) and IrNi-HD (53 $mV \cdot dec^{-1}$) were obtained at low overpotentials from LSV polarization curves at semi-steady-state (Figure S7). Obtained Tafel slopes were in the typical 35-50 $mV \cdot dec^{-1}$ range reported for hydrous IrO_x,[45,47,48] in contrast to ~ 60 $mV \cdot dec^{-1}$ reported for crystalline IrO_2.[49–51] IrNi-LY (0.006 cm^{-2}), IrNi-HD (0.003 cm^{-2}) and IrO_x (0.001 cm^{-2}) electrochemically active surface area (ECSA) were obtained from CV (0.5-0.6 V_{RHE}) at different scan rates (Figure S8). ECSA measurements suggest that IrNi-LY has a rougher surface than IrO_x. More significantly than the catalyst intrinsic activity is its stability during reaction, IrNi-LY showed a comparable degradation rate (15 $mV \cdot h^{-1}$) to IrO_x (11 $mV \cdot^{-1}$), much lower than the 160 $mV \cdot h^{-1}$ observed for IrNi-HD. The comparison of the intrinsic catalytic activity by LSV before and after the CP (10 $mA \cdot cm^{-2}$, 2 h) experiment confirmed the IrNi-LY and IrO_x catalysts stability against degradation (Figure S9).

To demonstrate that a high concentration of nickel at the surface compromises the overall stability of iridium against dissolution during OER, IrO_x, IrNi-LY and IrNi-HD catalysts were tested in a flow cell reactor coupled with an ICP, as described previously

in literature.[18] LSV measurements performed on a flow cell confirmed the comparable intrinsic activity between IrO_x and IrNi-LY observed in the conventional three electrode set up used for initial activity testing in this report (Figure S10a), in accordance with similar surface composition. Though the intrinsic activity of IrNi-LY resembles the activity of IrO_x when normalised to the electrode geometric surface area, the former catalyst contains half as much of iridium, which translates to 50 mV lower potential required to reach 10 $mA \cdot \mu g_{Ir}^{-1}$ compared to IrO_x when normalised to the iridium mass (Figure S10b and Figure S10c). Iridium and nickel dissolution were monitored during CP (10 $mA \cdot cm^{-2}$). Iridium and nickel mass dissolution obtained from ICP quantification can be found in Table S2. Slight iridium dissolution was observed for IrO_x, which seems not to affect the catalyst activity as observed by LSV measurements before and after CP. Iridium and nickel corrosion was detected for both IrNi-LY and IrNi-HD catalysts (Figure 6), thus, indicating that a small concentration of surface nickel was present on IrNi-LY. Iridium dissolution on IrNi-LY was comparable to that observed for IrO_x. However, the higher concentration of nickel at the IrNi-HD surface translated in considerably higher Ni corrosion compared to IrNi-LY, which in turn caused highly exposed iridium sites prone to dissolution.

Structural and electronic changes as a function of potential, from open circuit potential (OCP) to 1.3 V_{RHE} (0.1 V step, 5 min hold per potential), where followed through operando XAS spectroscopy at the Ir L_3 edge for IrNi-LY catalyst. XANES spectra (Figure 7) showed a gradual shift of the white line position accompanied with broadening towards higher binding energies with potential, which indicates that under OER Ir^{3+} sites oxidised to Ir^{4+},[34,37] with some researches suggesting the further oxidation to Ir^{5+} and Ir^{6+} under reaction conditions.[40,52,53] Strasser and co-workers[13] also assigned for $IrNiO_x$ the shift of the white line towards higher energy with potential to Ni leaching during OER, which shifted Ir d states to lower energy than oxygen 2p electrons, resulting in oxygen 2p holes.[13] In our case, the white line position shift with potential can be assigned to a combination of higher oxidation state of Ir centres and to surface Ni dissolution, as evidenced by ICP during OER. The adsorption spectra for IrNi-LY after reducing the potential from 1.3 V_{RHE} back to OCP recovered its original position and shape, indicating the stability of the catalyst and reversible redox processes.

Conclusions

The simultaneous addition of iridium chloride and nickel chloride precursors in a hydrothermal synthesis resulted in the formation of an IrNi mixed oxide catalyst with a metal homogeneous distribution (IrNi-HD). Whilst, layered IrO_x-$Ni(OH)_2$ (IrNi-LY) was obtained through sequential precipitation. The presence of Ir^{3+} and Ir^{4+} was confirmed by XPS and XAS for synthesised catalysts. EXAFS analysis confirmed a IrO_6 distortion compared to rutile IrO_2, with longer Ir-O bond distances in the first coordination shell and more disordered intermetallic bond distances in the second coordination shell (Ir-Ir and/or Ir-Ni).

Catalysts characterisation indicated that the surface of IrNi-LY is formed by an IrO_x-rich phase, while for IrNi-HD the surface is made of a combination of IrO_x and $Ni(OH)_2$. Surface composition has a great influence in the catalytic activity. IrNi-LY showed comparable catalyst activity and stability towards OER to an IrO_x catalyst synthesised following a similar procedure. However, due to the high concentration of surface $Ni(OH)_2$ fast deactivation and severe activity reduction was observed for IrNi-HD at short reaction times. Surface nickel is not stable against dissolution during OER, Ni corrosion produced highly undercoordinated iridium centres prone to corrosion, which eventually compromised the overall catalyst stability. *In situ* XAS analysis shows a shift in the white line position towards higher energy with potential, indicating that IrO_x partly oxidises during OER, cycling the potential back to OCP confirmed that structural and electronic transitions are reversible for IrO_x and IrNi-LY.

The activity and stability of highly active IrO_x catalysts can be maintained while lowering iridium concentration in mixed oxide catalysts through the formation of a surface IrO_x-rich phase, thus optimising iridium utilisation.

Author Information (ORCID)

Jonathan Ruiz Esquius 0000-0002-3809-5389

Gerardo Algara-Siller 0000-0002-1675-7273

Ioannis Spanos 0000-0001-5737-4992

Simon J. Freakley 0000-0002-6395-6646

Robert Schlögl 0000-0002-5163-1051

Graham J. Hutchings 0000-0001-8885-1560

Supporting Information

Rutile IrO_2 (Sigma Aldrich) XRD and XPS characterisation, rutile IrO_2 LSV (1.2 V_{RHE} - 1.8 V_{RHE}, 5 $mV \cdot s^{-1}$), CP (10 $mA \cdot cm^{-2}$) and CV (0.7 V_{RHE} - 1.4 V_{RHE} at 50 $mV \cdot s^{-1}$) measurements, Ir-O bond distances obtained from EXAFS fitting for IrO_x, IrNi-LY, IrNi-HD and IrO_2 and fitting parameters, cyclic voltammetry and Tafel slope for synthesised catalysts, LSV measurements in flow cell prior and after CP stability test, TGA measurements and iridium mass normalised LSV activity, *online* iridium and nickel dissolution during CP and operando XAS spectroscopy for IrNi-LY.

Acknowledgments

We would like to show our gratitude to the MaxNet Energy research consortium for its financial support. We would like to also thank Dr. Rosa Arrigo and Dr. Diego Gianolio from B18, Diamond Light Source at Harwell, for assisting us in the XAS spectroscopy experiment and providing the required sealed electrochemical cell. Finally, we would like to thank Dr. David J. Morgan for his assistance in XPS measurements.

Bibliography

(1) John Twidel, Anthony D. Weir. *Renewable Energy Sources*; Routledge, **2015**, 1-28.

(2) Vesborg, P. C. K.; Jaramillo, T. F. Addressing the Terawatt Challenge: Scalability in the Supply of Chemical Elements for Renewable Energy. *RSC Adv.* **2012**, *2* (21), 7933–7947.

(3) Rockström, J.; Steffen, W.; Noone, K.; Persson, Å.; Chapin III, F. S.; Lambin, E. F.; Lenton, T. M.; Scheffer, M.; Folke, C.; Schellnhuber, H. J.; Nykvist, B.; de Wit, C. A.; Hughes, T.; van der Leeuw, S.; Rodhe, H.; Sörlin, S.; Snyder, P. K.; Costanza, R.; Svedin, U.; Falkenmark, M.; Karlberg, L.; Corell, R. W.; Fabry, V. J.; Hansen, J.; Walker, B.; Liverman, D.; Richardson, K.; Crutzen, P.; Foley, J. A. A Safe Operating Space for Humanity. *Nature* **2009**, *461*, 472.

(4) Reier, T.; Pawolek, Z.; Cherevko, S.; Bruns, M.; Jones, T.; Teschner, D.; Selve, S.; Bergmann, A.; Nong, H. N.; Schlögl, R.; Mayrhofer, K. J. J.; Strasser, P. Molecular Insight in Structure and Activity of Highly Efficient, Low-Ir Ir–Ni Oxide Catalysts for Electrochemical Water Splitting (OER). *J. Am. Chem. Soc.* **2015**, *137* (40), 13031–13040.

(5) Moghaddam, R. B.; Wang, C.; Sorge, J. B.; Brett, M. J.; Bergens, S. H. Easily Prepared, High Activity Ir–Ni Oxide Catalysts for Water Oxidation. *Electrochem. Commun.* **2015**, *60*, 109–112.

(6) Nong, H. N.; Gan, L.; Willinger, E.; Teschner, D.; Strasser, P. IrOx Core-Shell Nanocatalysts for Cost- and Energy-Efficient Electrochemical Water Splitting. *Chem. Sci.* **2014**, *5* (8), 2955–2963.

(7) Nong, H. N.; Oh, H.-S.; Reier, T.; Willinger, E.; Willinger, M.-G.; Petkov, V.; Teschner, D.; Strasser, P. Oxide-Supported $IrNiO_x$ Core–Shell Particles as Efficient, Cost-Effective, and Stable Catalysts for Electrochemical Water Splitting. *Angew. Chem. Int. Ed.* **2015**, *54* (10), 2975–2979.

(8) Papaderakis, A.; Pliatsikas, N.; Prochaska, Ch.; Vourlias, G.; Patsalas, P.; Tsiplakides, D.; Balomenou, S.; Sotiropoulos, S. Oxygen Evolution at IrO_2 Shell–Ir−Ni Core Electrodes Prepared by Galvanic Replacement. *J. Phys. Chem. C* **2016**, *120* (36), 19995–20005.

(9) Pfeifer, V.; Jones, T. E.; Wrabetz, S.; Massué, C.; Velasco Vélez, J. J.; Arrigo, R.; Scherzer, M.; Piccinin, S.; Hävecker, M.; Knop-Gericke, A.; Schlögl, R. Reactive Oxygen Species in Iridium-Based OER Catalysts. *Chem. Sci.* **2016**, *7* (11), 6791–6795.

(10) Pfeifer, V.; Jones, T. E.; Velasco Vélez, J. J.; Massué, C.; Arrigo, R.; Teschner, D.; Girgsdies, F.; Scherzer, M.; Greiner, M. T.; Allan, J.; Hashagen, M.; Weinberg, G.; Piccinin, S.; Hävecker, M.; Knop-Gericke, A.; Schlögl, R. The Electronic Structure of Iridium and Its Oxides. *Surf. Interface Anal.* **2016**, *48* (5), 261–273.

(11) Pfeifer, V.; Jones, T. E.; Velasco Vélez, J. J.; Arrigo, R.; Piccinin, S.; Hävecker, M.; Knop-Gericke, A.; Schlögl, R. In Situ Observation of Reactive Oxygen Species Forming on Oxygen-Evolving Iridium Surfaces. *Chem. Sci.* **2017**, *8* (3), 2143–2149.

(12) Pfeifer, V.; Jones, T. E.; Velasco Vélez, J. J.; Massué, C.; Greiner, M. T.; Arrigo, R.; Teschner, D.; Girgsdies, F.; Scherzer, M.; Allan, J.; Hashagen, M.; Weinberg, G.; Piccinin, S.; Hävecker, M.; Knop-Gericke, A.; Schlögl, R. The Electronic Structure of Iridium Oxide Electrodes Active in Water Splitting. *Phys. Chem. Chem. Phys.* **2016**, *18* (4), 2292–2296.

(13) Nong, H. N.; Reier, T.; Oh, H.-S.; Gliech, M.; Paciok, P.; Vu, T. H. T.; Teschner, D.; Heggen, M.; Petkov, V.; Schlögl, R.; Jones, T.; Strasser, P. A Unique Oxygen Ligand Environment Facilitates Water Oxidation in Hole-Doped IrNiOx Core–Shell Electrocatalysts. *Nat. Catal.* **2018**, *1* (11), 841–851.

(14) Sasaki, K.; Kuttiyiel, K. A.; Barrio, L.; Su, D.; Frenkel, A. I.; Marinkovic, N.; Mahajan, D.; Adzic, R. R. Carbon-Supported IrNi Core–Shell Nanoparticles: Synthesis, Characterization, and Catalytic Activity. *J. Phys. Chem. C* **2011**, *115* (20), 9894–9902.

(15) Ruiz Esquius, J.; Morgan, D. J.; Spanos, I.; Hewes, D. G.; Freakley, S. J.; Hutchings, G. J. Effect of Base on the Facile Hydrothermal Preparation of Highly Active IrO_x Oxygen Evolution Catalysts. *ACS Appl. Energy Mater.* **2020**, *3* (1), 800–809.

(16) Genovese, C.; Schuster, M. E.; Gibson, E. K.; Gianolio, D.; Posligua, V.; Grau-Crespo, R.; Cibin, G.; Wells, P. P.; Garai, D.; Solokha, V.; Krick Calderon, S.; Velasco-Velez, J. J.; Ampelli, C.; Perathoner, S.; Held, G.; Centi, G.; Arrigo, R. Operando Spectroscopy Study of the Carbon Dioxide Electro-Reduction by Iron Species on Nitrogen-Doped Carbon. *Nat. Commun.* **2018**, *9* (1), 935.

(17) Ravel, B.; Newville, M. Athena, Artemis, Hephaestus: Data Analysis for X-Ray Absorption Spectroscopy Using IFEFFIT. *J. Synchrotron Radiat.* **2005**, *12* (4), 537–541.

(18) Spanos, I.; Auer, A. A.; Neugebauer, S.; Deng, X.; Tüysüz, H.; Schlögl, R. Standardized Benchmarking of Water Splitting Catalysts in a Combined Electrochemical Flow Cell/Inductively Coupled Plasma–Optical Emission Spectrometry (ICP-OES) Setup. *ACS Catal.* **2017**, *7* (6), 3768–3778.

(19) Xu, D.; Diao, P.; Jin, T.; Wu, Q.; Liu, X.; Guo, X.; Gong, H.; Li, F.; Xiang, M.; Ronghai, Y. Iridium Oxide Nanoparticles and Iridium/Iridium Oxide Nanocomposites: Photochemical Fabrication and Application in Catalytic Reduction of 4-Nitrophenol. *ACS Appl. Mater. Interfaces* **2015**, *7* (30), 16738–16749.

(20) Carnes, C. L.; Stipp, J.; Klabunde, K. J.; Bonevich, J. Synthesis, Characterization, and Adsorption Studies of Nanocrystalline Copper Oxide and Nickel Oxide. *Langmuir* **2002**, *18* (4), 1352–1359.

(21) Soler-Illia, G. J. de A. A.; Jobbágy, M.; Regazzoni, A. E.; Blesa, M. A. Synthesis of Nickel Hydroxide by Homogeneous Alkalinization. Precipitation Mechanism. *Chem. Mater.* **1999**, *11* (11), 3140–3146.

(22) Burattin, P.; Che, M.; Louis, C. Molecular Approach to the Mechanism of Deposition−Precipitation of the Ni(II) Phase on Silica. *J. Phys. Chem. B* **1998**, *102* (15), 2722–2732.

(23) Hall, D. S.; Lockwood, D. J.; Bock, C.; MacDougall, B. R. Nickel Hydroxides and Related Materials: A Review of Their Structures, Synthesis and Properties. *Proc. R. Soc. Math. Phys. Eng. Sci.* **2015**, *471* (2174), 20140792.

(24) Felix, C.; Maiyalagan, T.; Pasupathi, S.; Bladergroen, B.; Linkov, V. Synthesis and Optimisation of IrO_2 Electrocatalysts by Adams Fusion Method for Solid Polymer Electrolyte Electrolysers. *Micro Nanosyst.* **2012**, *4* (3), 186–191.

(25) Liao, P. C.; Chen, C. S.; Ho, W. S.; Huang, Y. S.; Tiong, K. K. Characterization of IrO_2 Thin Films by Raman Spectroscopy. *Thin Solid Films* **1997**, *301* (1), 7–11.

(26) Kim, H. W.; Shim, S. H.; Myung, J. H.; Lee, C. Annealing Effects on the Structural Properties of IrO_2 Thin Films. *Sel. Pap. Present. RIVA V-5th Iber. Vac. Meet.* **2008**, *82* (12), 1400–1403.

(27) Massué, C.; Huang, X.; Tarasov, A.; Ranjan, C.; Cap, S.; Schlögl, R. Microwave-Assisted Synthesis of Stable and Highly Active Ir Oxohydroxides for Electrochemical Oxidation of Water. *ChemSusChem* **2017**, *10* (9), 1958–1968.

(28) Willinger, E.; Massué, C.; Schlögl, R.; Willinger, M. G. Identifying Key Structural Features of IrO_x Water Splitting Catalysts. *J. Am. Chem. Soc.* **2017**, *139* (34), 12093–12101.

(29) Freakley, S. J.; Ruiz-Esquius, J.; Morgan, D. J. The X-Ray Photoelectron Spectra of Ir, IrO_2 and $IrCl_3$ Revisited. *Surf. Interface Anal.* **2017**, *49* (8), 794–799.

(30) Trasatti, S.; Buzzanca, G. Ruthenium Dioxide: A New Interesting Electrode Material. Solid State Structure and Electrochemical Behaviour. *J. Electroanal. Chem. Interfacial Electrochem.* **1971**, *29* (2), A1–A5.

(31) Panda, S. K.; Bhowal, S.; Delin, A.; Eriksson, O.; Dasgupta, I. Effect of Spin Orbit Coupling and Hubbard *U* on the Electronic Structure of IrO_2. *Phys. Rev. B* **2014**, *89* (15), 155102.

(32) Kahk, J. M.; Poll, C. G.; Oropeza, F. E.; Ablett, J. M.; Céolin, D.; Rueff, J.-P.; Agrestini, S.; Utsumi, Y.; Tsuei, K. D.; Liao, Y. F.; Borgatti, F.; Panaccione, G.; Regoutz, A.; Egdell, R. G.; Morgan, B. J.; Scanlon, D. O.; Payne, D. J. Understanding the Electronic Structure of IrO_2 Using Hard-X-Ray Photoelectron Spectroscopy and Density-Functional Theory. *Phys. Rev. Lett.* **2014**, *112* (11), 117601.

(33) McIntyre, N. S.; Cook, M. G. X-Ray Photoelectron Studies on Some Oxides and Hydroxides of Cobalt, Nickel, and Copper. *Anal. Chem.* **1975**, *47* (13), 2208–2213.

(34) Cruz, A. M.; Abad, Ll.; Carretero, N. M.; Moral-Vico, J.; Fraxedas, J.; Lozano, P.; Subías, G.; Padial, V.; Carballo, M.; Collazos-Castro, J. E.; Casañ-Pastor, N. Iridium Oxohydroxide, a Significant Member in the Family of Iridium Oxides. Stoichiometry, Characterization, and Implications in Bioelectrodes. *J. Phys. Chem. C* **2012**, *116* (8), 5155–5168.

(35) Biesinger, M. C.; Payne, B. P.; Lau, L. W. M.; Gerson, A.; Smart, R. St. C. X-Ray Photoelectron Spectroscopic Chemical State Quantification of Mixed Nickel Metal, Oxide and Hydroxide Systems. *Surf. Interface Anal.* **2009**, *41* (4), 324–332.

(36) Espinós, J. P.; Morales, J.; Barranco, A.; Caballero, A.; Holgado, J. P.; González-Elipe, A. R. Interface Effects for Cu, CuO, and Cu2O Deposited on SiO_2 and ZrO_2. XPS Determination of the Valence State of Copper in Cu/SiO_2 and Cu/ZrO_2 Catalysts. *J. Phys. Chem. B* **2002**, *106* (27), 6921–6929.

(37) Oakton, E.; Lebedev, D.; Povia, M.; Abbott, D. F.; Fabbri, E.; Fedorov, A.; Nachtegaal, M.; Copéret, C.; Schmidt, T. J. IrO_2-TiO_2: A High-Surface-Area, Active, and Stable Electrocatalyst for the Oxygen Evolution Reaction. *ACS Catal.* **2017**, *7* (4), 2346–2352.

(38) Zaman, W. Q.; Sun, W.; Tariq, M.; Zhou, Z.; Farooq, U.; Abbas, Z.; Cao, L.; Yang, J. Iridium Substitution in Nickel Cobaltite Renders High Mass Specific OER Activity and Durability in Acidic Media. *Appl. Catal. B Environ.* **2019**, *244*, 295–302.

(39) Godínez-Salomón, F.; Albiter, L.; Alia, S. M.; Pivovar, B. S.; Camacho-Forero, L. E.; Balbuena, P. B.; Mendoza-Cruz, R.; Arellano-Jimenez, M. J.; Rhodes, C. P. Self-Supported Hydrous Iridium–Nickel Oxide Two-Dimensional Nanoframes for High Activity Oxygen Evolution Electrocatalysts. *ACS Catal.* **2018**, *8* (11), 10498–10520.

(40) Mo, Y.; Stefan, I. C.; Cai, W.-B.; Dong, J.; Carey, P.; Scherson, D. A. *In Situ* Iridium LIII-Edge X-Ray Absorption and Surface Enhanced Raman Spectroscopy of

Electrodeposited Iridium Oxide Films in Aqueous Electrolytes. *J. Phys. Chem. B* **2002**, *106* (14), 3681–3686.

(41) Massué, C.; Pfeifer, V.; Huang, X.; Noack, J.; Tarasov, A.; Cap, S.; Schlögl, R. High-Performance Supported Iridium Oxohydroxide Water Oxidation Electrocatalysts. *ChemSusChem* **2017**, *10* (9), 1943–1957.

(42) Spöri, C.; Kwan, J. T. H.; Bonakdarpour, A.; Wilkinson, D. P.; Strasser, P. The Stability Challenges of Oxygen Evolving Catalysts: Towards a Common Fundamental Understanding and Mitigation of Catalyst Degradation. *Angew. Chem. Int. Ed.* **2017**, *56* (22), 5994–6021.

(43) Jamesh, M.-I.; Sun, X. Recent Progress on Earth Abundant Electrocatalysts for Oxygen Evolution Reaction (OER) in Alkaline Medium to Achieve Efficient Water Splitting – A Review. *J. Power Sources* **2018**, *400*, 31–68.

(44) Spöri, C.; Briois, P.; Nong, H. N.; Reier, T.; Billard, A.; Kühl, S.; Teschner, D.; Strasser, P. Experimental Activity Descriptors for Iridium-Based Catalysts for the Electrochemical Oxygen Evolution Reaction (OER). *ACS Catal.* **2019**, *9* (8), 6653–6663.

(45) Ouattara, L.; Fierro, S.; Frey, O.; Koudelka, M.; Comninellis, C. Electrochemical Comparison of IrO_2 Prepared by Anodic Oxidation of Pure Iridium and IrO_2 Prepared by Thermal Decomposition of H_2IrCl_6 Precursor Solution. *J. Appl. Electrochem.* **2009**, *39* (8), 1361–1367.

(46) Juodkazytė, J.; Šebeka, B.; Valsiunas, I.; Juodkazis, K. Iridium Anodic Oxidation to Ir(III) and Ir(IV) Hydrous Oxides. *Electroanalysis* **2005**, *17* (11), 947–952.

(47) Abbott, D. F.; Lebedev, D.; Waltar, K.; Povia, M.; Nachtegaal, M.; Fabbri, E.; Copéret, C.; Schmidt, T. J. Iridium Oxide for the Oxygen Evolution Reaction: Correlation between Particle Size, Morphology, and the Surface Hydroxo Layer from Operando XAS. *Chem. Mater.* **2016**, *28* (18), 6591–6604.

(48) Smith, R. D. L.; Sporinova, B.; Fagan, R. D.; Trudel, S.; Berlinguette, C. P. Facile Photochemical Preparation of Amorphous Iridium Oxide Films for Water Oxidation Catalysis. *Chem. Mater.* **2014**, *26* (4), 1654–1659.

(49) Oscar Diaz-Morales; Stefan Raaijman; Ruud Kortlever; Patricia J. Kooyman; Tim Wezendonk; Jorge Gascon; W. T. Fu; Marc T. M. Koper. Iridium-Based Double Perovskites for Efficient Water Oxidation in Acid Media. *Nat. Commun.* **2016**, *7* (1).

(50) Reier, T.; Oezaslan, M.; Strasser, P. Electrocatalytic Oxygen Evolution Reaction (OER) on Ru, Ir, and Pt Catalysts: A Comparative Study of Nanoparticles and Bulk Materials. *ACS Catal.* **2012**, *2* (8), 1765–1772.

(51) Gao, J.; Xu, C.-Q.; Hung, S.-F.; Liu, W.; Cai, W.; Zeng, Z.; Jia, C.; Chen, H. M.; Xiao, H.; Li, J.; Huang, Y.; Liu, B. Breaking Long-Range Order in Iridium Oxide by

Alkali Ion for Efficient Water Oxidation. *J. Am. Chem. Soc.* **2019**, *141* (7), 3014–3023.

(52) Binninger, T.; Fabbri, E.; Patru, A.; Garganourakis, M.; Han, J.; Abbott, D.; Sereda, O.; Kötz, R.; Menzel, A.; Nachtegaal, M.; Schmidt, T. Electrochemical Flow-Cell Setup for In Situ X-Ray Investigations: I. Cell for SAXS and XAS at Synchrotron Facilities. *J. Electrochem. Soc.* **2016**, *163*, H906–H912.

(53) Cheng, J.; Yang, J.; Kitano, S.; Juhasz, G.; Higashi, M.; Sadakiyo, M.; Kato, K.; Yoshioka, S.; Sugiyama, T.; Yamauchi, M.; Nakashima, N. Impact of Ir-Valence Control and Surface Nanostructure on Oxygen Evolution Reaction over a Highly Efficient Ir–TiO_2 Nanorod Catalyst. *ACS Catal.* **2019**, *9* (8), 6974–6986.

Figures

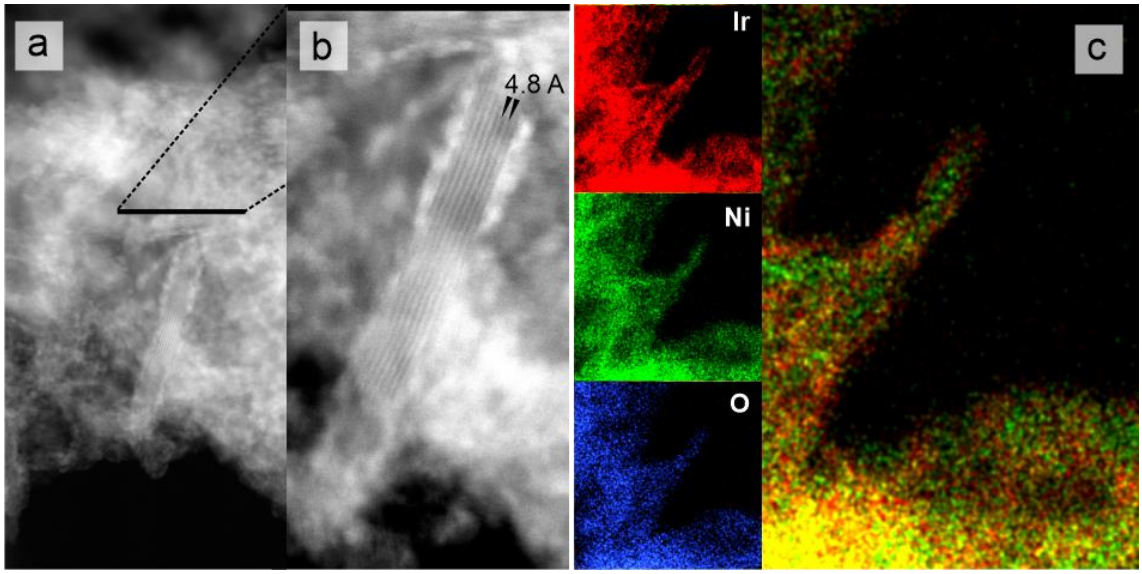

Figure 1. a) Dark field scanning TEM image for IrNi-LY. b) Higher magnification image of a) showing the layered structure of $Ni(OH)_2$. c) Energy dispersive x-ray spectroscopy composite image from Ni and Ir signals. From this characterisation it is possible to derive that the material on the surface of layered $Ni(OH)_2$ is an Ir-rich phase. Insets (brightness and contrast enhanced) show the colour code for each element. Image width of a) 50 nm, b) 19 nm and c) 50 nm.

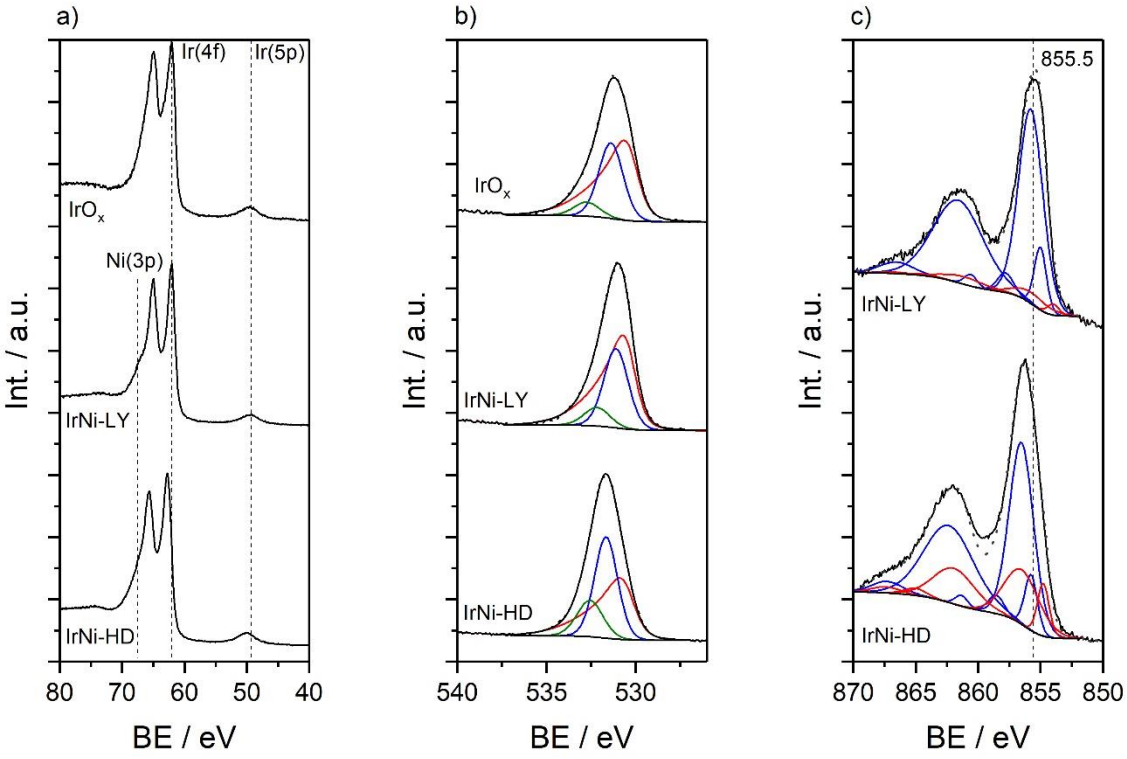

Figure 2. a) Ir(4f), b) O(1s) and c) Ni(2p) XPS characterisation for IrO_x, IrNi-LY and IrNi-HD. Red fitting corresponds to the oxide form, blue fitting to the hydroxide form and green fitting to water/carbonate. Obtained fitting is represented with a dotted line.

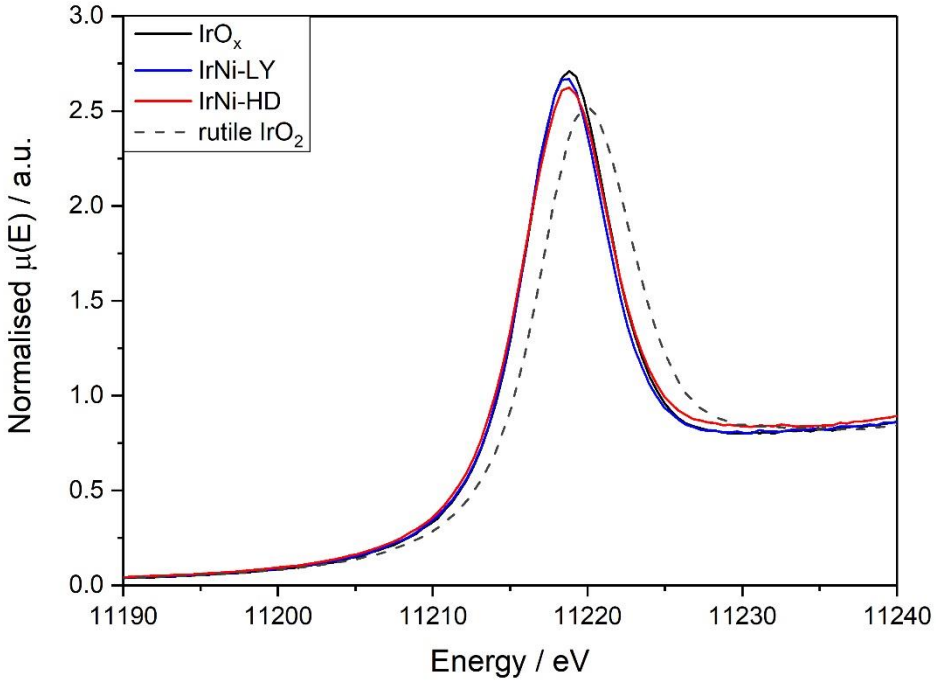

Figure 3. Ir L_3 edge XAS data for synthesised IrO_x, IrNi-HD, IrNi-LY and commercial rutile IrO_2.

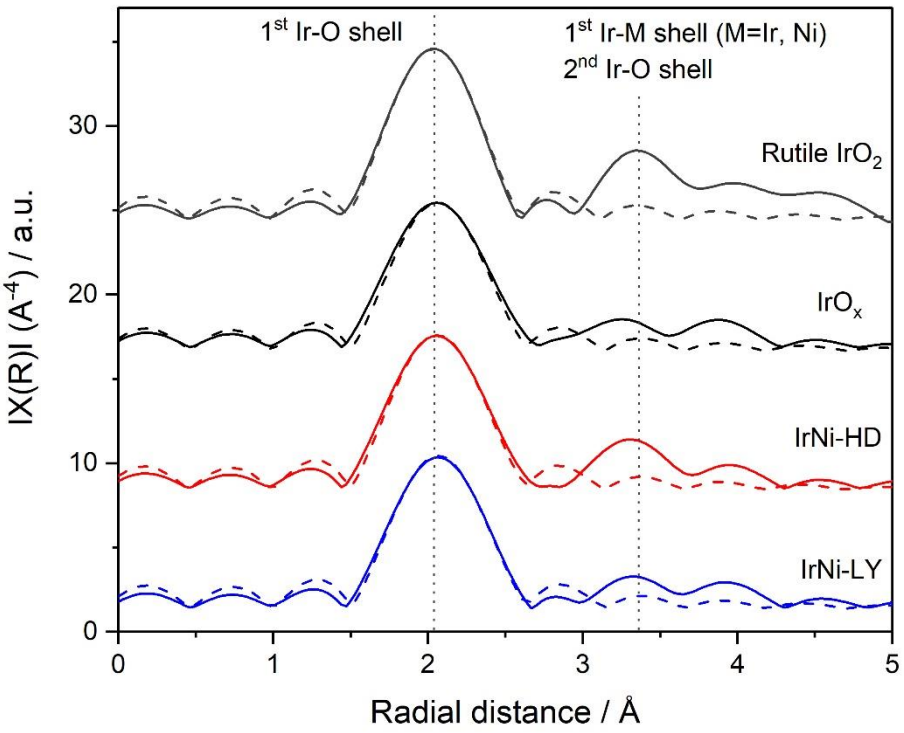

Figure 4. EXAFS signal obtained from the fourier transform of XAS with a k weight 3 for synthesised IrOx, IrNi-HD, IrNi-CS and commercial rutile IrO_2 (experimental data and fits represented with a solid and dahsed lines respectively, note that only the first coordination shell was used in the fitting).

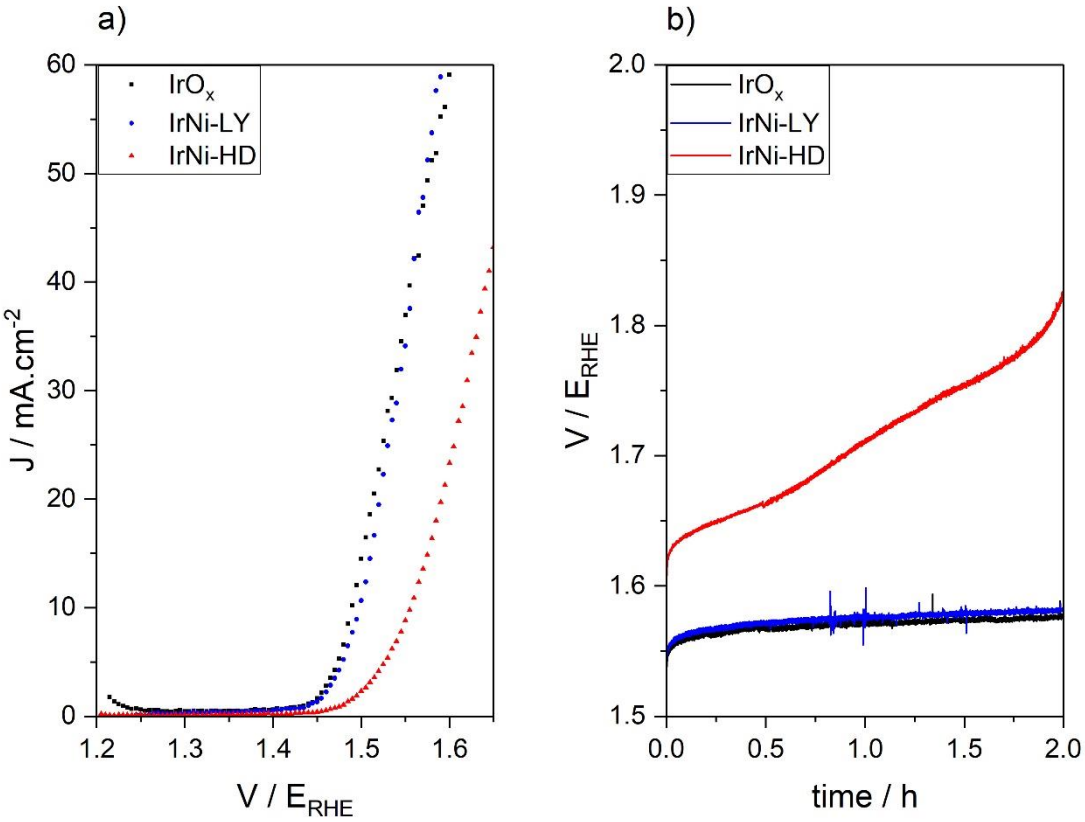

Figure 5. a) Intrinsic catalytic activity towards OER determined by LSV (1.20 V_{RHE} to 1.65 V_{RHE} at 5 mV·s^{-1}) b) catalyst stability determined by CP (10 mA·cm^{-2}, 2 h).

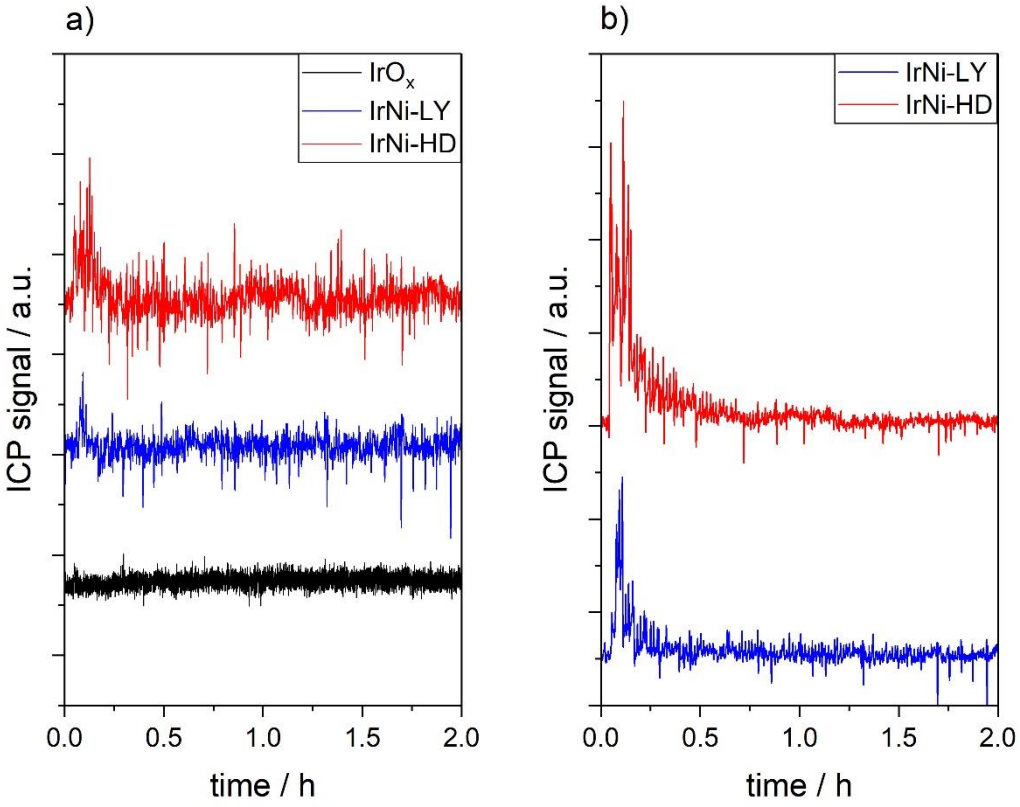

Figure 6. a) iridium and b) nickel online dissolution detected by ICP during chronopotentiometry (10 mA·cm^{-1}, 2h) in a flow cell.

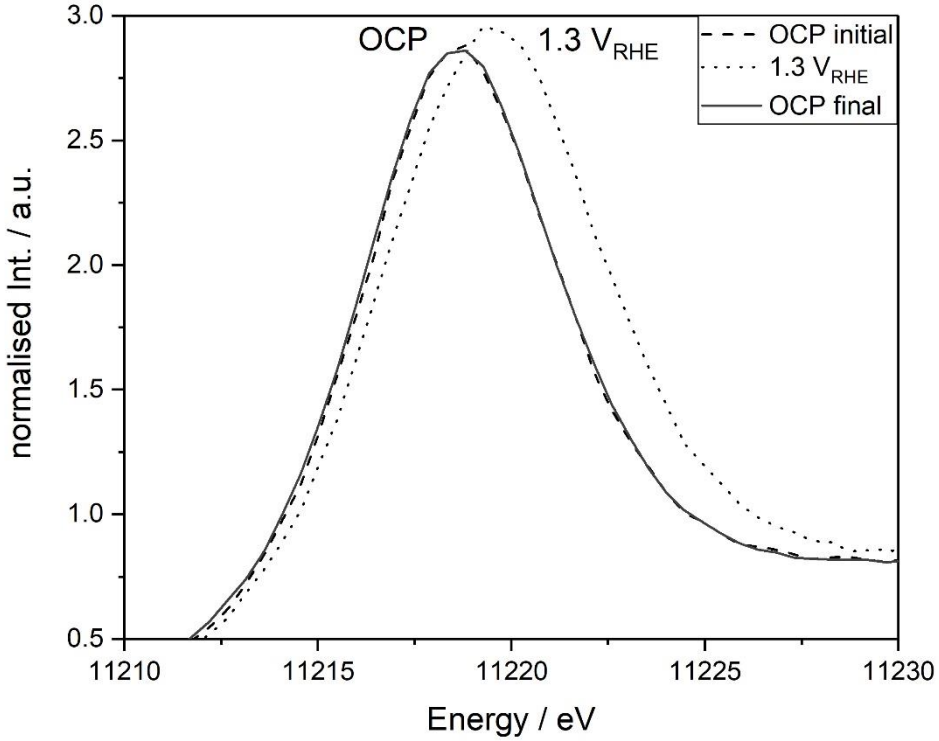

Figure 7. Operando XAS spectroscopy for IrNi-LY catalyst at Ir L_3 edge, initial and final white position after cycling the potential from OCP to 1.3 V_{RHE} and back to OCP, compared to white line at 1.3 V_{RHE}.

Tables

Table 1. Surface iridium and nickel atomic ratio obtained from the Ir($4d_{5/2}$) and Ni($2p_{3/2}$) peak quantification and surface oxygen speciation (oxide, hydroxide and water/carbonates) obtained from the O(1s) by XPS.

Catalyst	Ir at. %	Ni at. %	O / oxide %	O / OH %	O / H_2O-CO_3^{-2} %
IrO_x	100	0	59	34	7
IrNi-HD	47	53	44	40	16
IrNi-LY	60	40	57	34	9

Table 2. XAS data for synthesised IrO_x, IrNi-HD, IrNi-LY and *commercial rutile IrO_2 catalysts. 2 Ir-O_{ax} (axial) and 4 Ir-O_{eq} (equatorial) bonds were used in the fitting to obtain the Ir-O_{av} (average) bond distance.

Catalyst	Absorption edge energy, eV	Ir-O_{ax} bond distance, Å	Ir-O_{eq} bond distance, Å	Ir-O_{av} bond distance, Å
*Rutile IrO_2	11220.0	1.96	1.99	1.98(7)
IrO_x	11218.8	1.99	2.02	2.01(3)
IrNi-HD	11218.8	1.99	2.03	2.01(2)
IrNi-LY	11218.7	2.00	2.03	2.02(2)

Table 3. Catalytic performance of IrO_x, IrNi-HD and IrNi-LY towards OER.

catalyst	Electrode area norm. activity (η = 0.35 V): J / mA·cm^{-2}	Ir mass norm. activity (η = 0.35 V): J / mA·cm^{-2}·µg$_{Ir}^{-1}$	Degradation rate mV·h^{-1}
IrO_x	51.5	3.0	11
IrNi-LY	53.6	5.6	15
IrNi-HD	16.5	1.8	160